Progress in Natural Science: Materials International 26 (2016) 325–333

HOSTED BY

Contents lists available at ScienceDirect

Progress in Natural Science: Materials International

journal homepage: www.elsevier.com/locate/pnsmi

Original Research

Structural, electrical, dielectric and magnetic properties of Mn-Nd substituted $CoFeO_3$ nano sized multiferroics

Abdul Aziz [a,*], E. Ahmed [a], Muhammad Naeem Ashiq [b], Muhammad Azhar Khan [c,*], Nazia Karamat [b], Irshad Ali [a]

[a] Department of Physics, Bahauddin Zakariya University, Multan, Pakistan
[b] Institute of Chemical Sciences, Bahauddin Zakariya University, Multan, Pakistan
[c] Department of Physics, The Islamia University of Bahawalpur, Bahawalpur-63100, Pakistan

ARTICLE INFO

Article history:
Received 29 November 2015
Received in revised form
19 June 2016
Accepted 20 June 2016
Available online 10 August 2016

Keywords:
Nanostructured materials
XRD
Dielectric properties
Electrical properties
Magnetic properties

ABSTRACT

A series of $Mn_xCo_{1-x}Fe_{1-y}Nd_yO_3$ (where x=0.0–1.0 & y=0.0–0.1) multiferroic nanocrystals was synthesized via sol-gel auto-combustion technique. The structure was confirmed by X-ray diffraction (XRD) while morphology was investigated by scanning electron microscopy (SEM). The electrical resistivity was observed to increase from 2.14×10^7 to 8.77×10^9 Ω-cm and activation energy was found to increase from 0.64 to 0.75 eV, while the drift mobility decreased from 4.75×10^{-13} to 1.27×10^{-15} $cm^2 V^{-1} S^{-1}$ by the substitution of Mn and Nd contents. The dielectric constant, dielectric loss and dielectric loss factor decrease with frequency and Mn-Nd contents. The saturation magnetization was increased from 34 to 70 emu g^{-1} while the coercivity decreased from 705 to 262 Oe with the increase of substituents. The increase in electrical resistivity and saturation magnetization while decrease in dielectric parameters and coercivity make these nanomaterials suitable for applications in microwave devices and longitudinal magnetic recording media.

1. Introduction

Ferrite materials have great importance due to their applications in high density recording media, microwave devices, drug delivery, hyper thermal cancer treatment and magneto-optical devices [1]. Multiferroic materials with ferroelectric (FE) and ferromagnetic (FM) properties offer potential applications for functional devices. The fundamental requirement is the presence of FM and FE simultaneously above room temperature in a single phase material [2]. Aside from its fundamental importance, the mutual control of electric and magnetic properties is of significant interest for their applications in magnetic storage media and spintronics [3,4]. Few materials with ferroelectricity and ferromagnetism are reported but the coupling between electric and magnetic properties is not always large enough [5]. Such materials continue to attract great fundamental scientific interest in past several years due to their potential applications in multifunctional devices such as the data storage, magnetic filter and sensors.

Due to rapid development in the field of telecommunication, the operational frequencies of electronic devices increase to GHz range. Owing to low AC electrical conductivity, low eddy current and dielectric losses of these polycrystalline ferrite materials are particularly well suited for their use in high frequency applications. The experimental measurement of the dielectric properties and DC electrical resistivity reveal valuable information about the behavior of the free and localized charge carriers. This leads to appropriate explanation and understanding of the mechanism of electric conduction in the studied samples.

The main focus of the present work is to enhance the electrical resistivity and to reduce the eddy current loss and dielectric parameters. The electrical and dielectric properties are dependent on their structure, particle size, composition, cation distribution and method of synthesis [6,7]. Several methods have been employed for the synthesis of such materials including solid state reaction [8], hydrothermal [9], sol–gel auto-combustion [10,11], co-precipitation [12], citrate precursor technique [13], thermal plasma [14], pulsed wire discharge [15], etc. In the present work, we have used the sol-gel auto- combustion method which is better to obtain the nano-size materials as compared to others. It is well known that the sol-gel method has been proved to be one of the most effective routes to realize the low temperature sintering of these materials. The substitution or complete replacement of A or B site elements can change the oxygen vacancies in these materials which play important role in the electrical and dielectric properties [16,17].

* Corresponding authors.
E-mail addresses: aziz_bloch@hotmail.com (A. Aziz), azhar.khan@iub.edu.pk (M.A. Khan).
Peer review under responsibility of Chinese Materials Research Society.

http://dx.doi.org/10.1016/j.pnsc.2016.06.003

Recently Rayaprol et. al reported $MnFeO_3$ and investigated its structural and magnetic properties [18]. The material shows ferromagnetic nature at 300 K and anti-ferromagnetic behavior at round 36 K. Similar type of material $MnFeO_3$ has also been synthesized in the recent year [19]. The cobalt is in the same period of the periodic table as that of manganese and also has three unpaired electrons which can generate the magnetic properties in the material synthesized in the present work. The electrical properties in these materials depends upon the electron transfer between ferric and ferrous ion as well as the hole transfer between Mn^{2+} to Mn^{3+}.

The main purpose of the present work is to enhance the electrical resistivity and saturation magnetization while to reduce the dielectric parameters and coercivity so that they can be used for microwave devices and high density recording media applications. Owing to above mentioned reasons the cobalt based $CoFeO_3$ material has been chosen. In order to make these materials more viable for applications, Mn^{2+} and Nd^{3+} are selected to substitute for Co^{2+} and Fe^{3+}, respectively. Because the third ionization energy of Mn (3248 kJ mol^{-1}) is higher than that of Co (3232 kJ mol^{-1}) which mean that the energy required to hole transfer between Mn^{2+} to Mn^{3+} is greater than Co^{2+} to Co^{3+}. This may help in increasing the electrical resistivity of the synthesized materials. The Mn^{2+} has (5) higher unpaired electrons as compared to Co^{2+} (2) which can help in enhancing the magnetic properties as well.

2. Experimental technique

2.1. Chemicals

The chemicals used for the synthesis of $Mn_xCo_{1-x}Fe_{1-y}Nd_yO_3$ nano-crystallites were $Co(NO_3)_3$ (Sigma–Aldrich, 97%), $Fe(NO_3)_3 0.9H_2O$ (Sigma–Aldrich, 98%), $MnCl_2 0.4H_2O$ (Sigma–Aldrich, 98%), $Nd_2O_3 0.6H_2O$ (Riedel–de Haen, 98%), Citric acid (Merck, 98%), Aqueous NH_3 (BDH,35% purity). All the chemicals were used as received without further purifications.

2.2. Synthesis procedure

$Mn_xCo_{1-x}Fe_{1-y}Nd_yO_3$ (where x=0.0,0.2,0.4,0.6,0.8,1.0 and y=0.00,0.02,0.04,0.06,0.08,0.1) nanomaterials were prepared by the chemical sol-gel auto-combustion method as reported elsewhere [20]. The stoichiometric amounts of metal salts were dissolved in deionized water and were mixed in a beaker. The pH of mixed solutions was adjusted at 7 by adding 2 M ammonia solution. The citric acid was added in the mixture keeping the ratio between metal to chelating agent (citric acid) 1:1.5. The solution was then evaporated slowly at 80 °C until it was converted to gel. The gel was then burnt at 300 °C which convert into black powder. Finally the powder was calcined at 800 °C for 7 h. The calcined powder was pressed into pellets of 10 mm diameter and of thickness 3 mm to measure the dielectric parameters and dc electrical resistivity. The both surfaces of the pellets were coated with silver paste to make electrodes for the measurement of dielectric properties.

2.3. Characterization

PANAlytical X-ray diffractometer was used for XRD analysis to confirm the phase formation which uses CuK_α as a radiation source ($\lambda=1.54056$ Å). The experiments were performed in the 2θ range of $20-70^\circ$ with step size of 0.02° at 45 kV/40 mA. A Ni-filter has been used to absorb CuK_β. Scanning electron microscopy (SEM) was carried out by using Hitachi S4800 FE-SEM to study the surface morphology. The DC resistivity measurement was carried out by two-point probe method using the source meter-Keithley model 2400. The dielectric measurement was done at room temperature using an Agilent impedance analyzer model E499IARF over the frequency range of 1 MHz–3 GHz. The hysteresis loops were measured by using vibrating sample magnetometer (VSM) model Lake shore$^-$74,071.

2.4. Calculations

The bulk density (ρ_m) was calculated using the following relation:

$$\rho_m=\frac{m}{\pi r^2 h} \tag{1}$$

where 'm' is the mass of the pellet, 'r' is the radius of the pellet, and 'h' is the thickness of the pellet. The X-ray diffraction data was used to calculate crystallite size, lattice constant, cell volume, X-ray density and porosity. The average crystallite size (D) was determined by using Scherrer's formula:

$$D=\frac{K\lambda}{\beta\ cos\ \theta} \tag{2}$$

where λ is the wavelength of the X-rays used, β is the full width at half maxima (FWHM), θ is Bragg's angle and K is the scherrer constant which is equal to 0.9 [21]. The lattice constant and cell volume were calculated by using following relation:

$$V_{cell}=a\times b\times c \tag{3}$$

The lattice parameters i.e. a, b and c were determined using cell software (Cell version 5.0 (copyright by K. Dwight, USA, 1986). X-Ray density was calculated by using Eq. (4):

$$\rho_{x-ray}=\frac{ZM}{N_{AV_{cell}}} \tag{4}$$

where M is the molar mass, the value of Z (number of formula units per unit cell) is 4 for orthorhombic system. The porosity was calculated by using following equation:

$$P=1-\frac{\rho_m}{\rho_{X-ray}} \tag{5}$$

The relative complex permittivity is the dielectric response of a crystalline solid that can be explained by the following equation:

$$\varepsilon^*(\omega)=\varepsilon'(\omega)+j\varepsilon''(\omega) \tag{6}$$

$\varepsilon'(\omega)$ shows the capacitance (stored energy), and $\varepsilon''(\omega)$ is directly related to the dielectric dissipated energy. Numerous dielectric parameters were calculated with the help of the following equation:

$$\varepsilon'=\frac{Cd}{A} \tag{7}$$

In the above equation C is the capacitance of the pellet (in farad), d is the thickness of the pellet (in meter) and A is the area of the pellets. The dielectric dissipation factor was calculated as follows:

$$\varepsilon''=\varepsilon' \tan\ \delta \tag{8}$$

The ac electrical conductivity (σ_{AC}) of the samples was calculated from the dielectric data using the following relation:

$$\sigma_{AC}=2\pi f \epsilon_o \varepsilon'' \tag{9}$$

where 2π and ε_0 are constants and f is the frequency and ε'' is dielectric loss. The DC electrical resistivity (ρ) was calculated using the formulae:

$$\rho=\frac{RA}{h} \tag{10}$$

where R is the resistance, h is the thickness of the sample, A (πr^2) is the area of electrode in contact with the sample. The drift mobility was determined by using the following relation:

$$\mu_d=\frac{\sigma_{DC}}{ne} \tag{11}$$

where e is the charge of electron, σ_{DC} is conductivity and n is the concentration of charge carrier and can be calculated from the well-known equation:

$$n=\frac{N_A\rho_m P_{Fe}}{M}$$

where N_A is Avogadro's number, ρ_m is the measured bulk density of sample, P_{Fe} is the number of iron atoms in the chemical formula and M is the molecular weight of the samples.

The values of activation energies were calculated from the slope of Arrhenius plots and are given by the following relation:

$$\rho=\rho_{\circ}\exp\left(\frac{E_a}{k_B T}\right) \tag{12}$$

where ρ is the resistivity at temperature T. $\rho_{\blacklozenge}$ is the pre-exponentional factor, E_a is the activation energy and k_B is the Boltzmann's constant.

3. Results and discussion

3.1. Structural analysis

Powder XRD patterns for all the annealed samples are shown in Fig. 1. The XRD peaks of all the samples perfectly match with the standard pattern (ICSD-00-015-0148). This indicates that all the samples are single phase orthorhombic. The perfect match of XRD patterns with the standard pattern for all the synthesized samples $Mn_xCo_{1-x}Fe_{1-y}Nd_yO_3$ (x=0.0,0.2,0.4,0.6,0.8,1.0), (y=0.00,0.02,0.04, 0.06,0.08,0.1) confirm the successful substitution of Nd^{3+} at Fe^{3+} and Co^{2+} at Mn^{2+} sites. Cell volume is found to increase from 183.32 to 238.97 Å^3 with the increase of both substituents (Table 1). This increase in cell volume confirm the complete and successful replacement of smaller ionic radii (Fe^{3+} (0.64 Å) and Co^{2+} (0.74)) ions by relatively larger ionic radii Nd^{3+} (1.109 Å) and Mn^{2+} (0.80 Å) ions, respectively at appropriate positions. Further confirmation of successful and simultaneous double ions substitution of

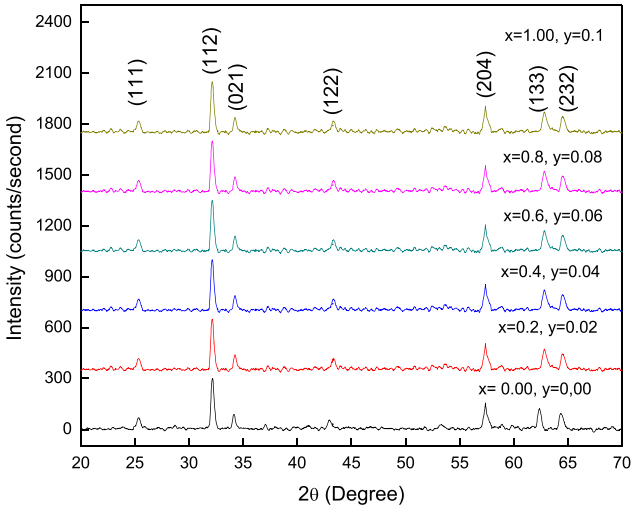

Fig. 1. XRD patterns of Mn-Nd co-substituted CFO magnetic nanomaterials.

Table 1
Lattice constants (a, b and c), cell volume, x-ray density, bulk density, porosity and grain size.

Parameter	x=0, y=0	x=0.2, y=0.02	x=0.4, y=0.04	x=0.6, y=0.06	x=0.8, y=0.08	x=1.0, y=0.1
a(Å)	4.92	5.28	5.63	5.66	5.76	5.32
b(Å)	5.23	5.22	5.40	5.38	5.56	5.68
c(Å)	7.11	7.10	7.23	7.34	7.29	7.89
V(Å^3)	183.32	196.32	220.16	223.89	234.20	238.97
$\rho_{x\text{-}ray}$ (g/cm^3)	5.90	5.60	5.00	4.90	4.70	4.60
ρ_m (g/cm^3)	4.33	4.28	4.25	4.21	4.17	4.16
Porosity (%)	26.61	23.57	15.00	14.08	11.27	9.56

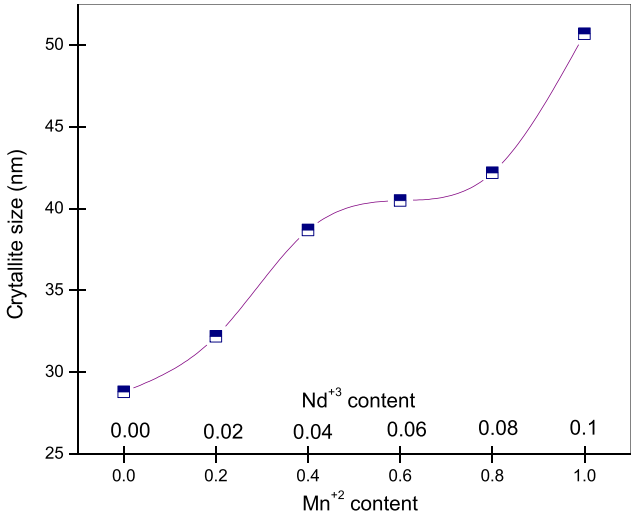

Fig. 2. Variation in crystallite size as a function of dopant.

Co^{2+} and Fe^{3+} with Mn^{2+} and Nd^{3+} can be observed from X-ray density, bulk density and porosity trends with variables x and y contents. The value X-ray density is relatively greater than that of bulk density. This indicates the presence of pores in these nanocrystallites. The porosity values are found in the range 9.56–26.61% (Table 1). The crystallite size calculated by Scherrer's formula is found in the range of 24–39 nm as shown in Fig. 2 which is smaller compared to 30–50 nm which was reported in literature [22].

3.2. Surface analysis

The surface morphologies of the samples were investigated by FE-SEM analysis and their images are shown in Fig. 3. All the samples have good crystallinity which is evidenced by the clear morphologies and distinct boundaries of the grains with homogeneous grain size distribution. It can be seen that the co-doped $Mn_xCo_{1-x}F_{1-y}Nd_yO_3$ (MCFNO) have well-grown larger grains and denser morphology as compared to un-substituted sample. The grain morphology looks like spheres initially then turns into rods with increasing dopants contents. This typical shape is favorable for microwave absorbing purposes [23]. The grains grow larger in size ($\lesssim$50 nm) with increasing concentration of Mn-Nd. A close examined of these micrographs clearly indicates that some particles agglomerate into larger particles. The chemical reaction during the sintering process plays a very crucial role for the formation of these agglomerates [24].

3.3. DC electrical resistivity

The DC electrical resistivity was measured by two point probe method in the temperature range of 298–573 K.

3.3.1. Room temperature electrical resistivity

It is observed from the values of resistivity given in Table 2 that the room temperature resistivity increases with the increase in Mn-Nd contents from 2.14×10^7 to 8.77×10^9 Ω-cm. The conduction mechanism in such materials is due to transfer of electrons from ferrous to ferric ions at octahedral site as well as holes transfer from Mn^{2+} to Mn^{3+}. It has been reported that Nd and Mn both ions occupy the octahedral site [25]. The concentration of Fe^{3+} ions gradually decreases at B-sites when Nd is substituted in place of iron. The hopping rate of electron transfer will also decrease with the decrease of Fe^{3+} ions concentration. As a result, it enhances the dc resistivity with the increase of Mn-Nd concentration. A possible reason for increase in resistivity by increasing Mn-Nd is due to the fact that the occupancy of Mn-Nd ions at B-sites may increase the separation between Fe^{3+} and Fe^{2+} ions in proportion to its ionic radii which is in consistent with the variation of lattice constant versus Mn-Nd contents. Since the hopping of electrons between ferrous and ferric ions is restricted and as a result both resistivity and activation energy increase. These results are consistent with the results reported by many authors [26,27]. It has reported that the Mn^{2+} can be changed to Mn^{3+} and produce holes [28,29]. Now the conductivity is due to transfer of electrons as well as holes but the transfer of hole is more difficult as compared to electrons and as a result the resistivity enhanced. The third ionization energy of cobalt is smaller than that of manganese which indicates that the holes transfer in Co^{2+} to Co^{3+} is easier than that of Mn^{2+} to Mn^{3+} and consequently the resistivity enhanced. The conduction mechanism can be written as:

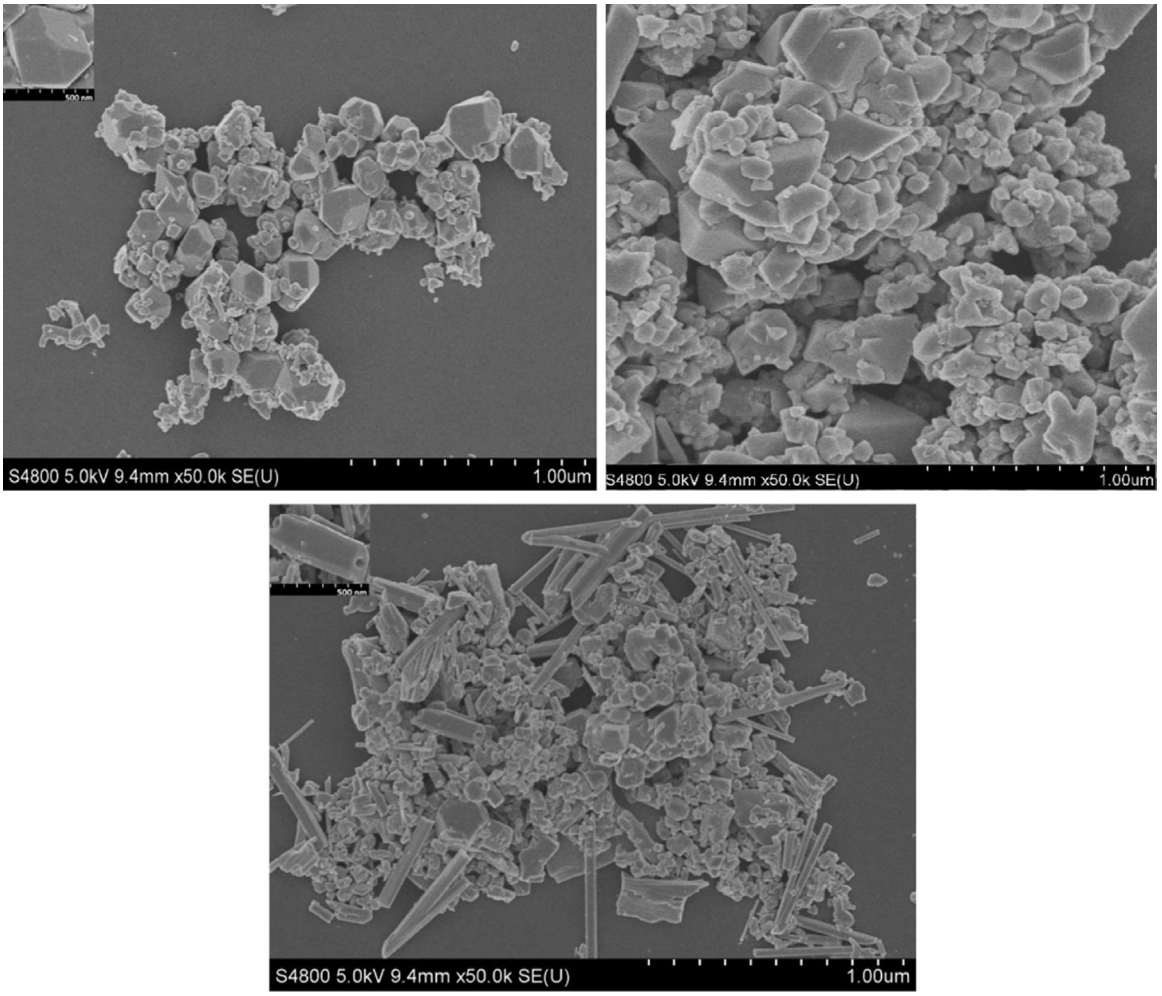

Fig. 3. SEM images of Mn-Nd co-substituted CFO magnetic materials.

Table 2
Dielectric constant, dielectric loss, tangent loss, AC conductivity, resistivity, drift mobility, n and coercivity.

Parameter	$x=0$, $y=0$	$x=0.2$, $y=0.02$	$x=0.4$, $y=0.04$	$x=0.6$, $y=0.06$	$x=0.8$, $y=0.08$	$x=1.0$, $y=0.1$
Dielectric Constant	41.87	31.08	30.86	29.58	24.30	10.53
Dielectric Loss	5.65	4.82	4.41	3.73	3.28	2.55
Tan δ	0.13	0.16	0.11	0.12	0.10	0.09
σ_{ac} $(\Omega\text{-cm})^{-1}$	3.14E−04	2.68E−04	2.45E−04	2.07E−04	1.82E−04	1.42E−04
ρ (Ω-cm)	2.14E07	9.17E07	2.42E08	8.9E08	3.56E09	8.77E09
$\mu_d(cm^2\ V^{-1}\ S^{-1})$	4.75E−13	1.13E−13	4.36E−14	1.21E−14	3.09E−15	1.27E−15
n	0.809	0.811	0.816	0.840	0.700	0.760
Coercivity (Oe)	705	614	550	525	325	262

$Fe^{2+} \leftrightarrow Fe^{3+} + e^-$

$Mn^{3+} + e^- \leftrightarrow Mn^{2+}$

Combining the above two equations.

$Mn^{2+} + Fe^{3+} \leftrightarrow Mn^{3+} + Fe^{2+}$

3.3.2. Temperature dependent DC resistivity

Temperature dependent dc resistivity of $Mn_xCo_{1-x}Nd_yFe_{(1-y)}O_3$ multiferroics (x=0.0–1.0, y=0.00–0.1) has been measured in the temperature range of 298–573 K. The Arrhenius plots are shown in Fig. 4 and activation energy was calculated from the slopes of these plots. It can be observed that the dc resistivity decreases exponentially with temperature for all the samples indicating the semiconducting type behavior of these samples as shown in the inset of Fig. 4. A similar trend of the DC resistivity was reported earlier by many researchers [30,31]. The steeper slope of all the samples of $Mn_xCo_{1-x}Nd_yFe_{(1-y)}O_3$ multiferroics may be attributed to thermally activated mobility of charge carriers but not to thermally activated creation of these carriers. The calculated values of activation energy (E_a) are shown in Fig. 5 as a function of Mn-Nd contents. It can be concluded that the sample with higher resistivity has higher values of activation energies and vice versa [32]. Since the resistivity has been found to increase with the substitution concentration so rise in activation energies with both Mn and Nd addition is expected.

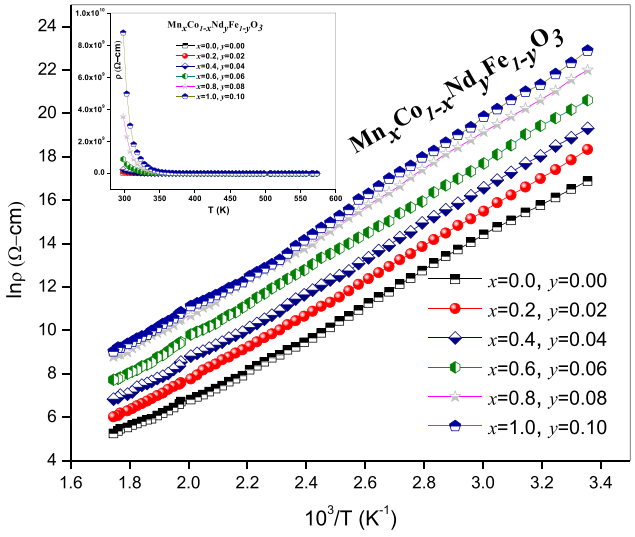

Fig. 4. Arrhenius plots and resistivity versus T(K) (inset) for Mn-Nd co-substituted CFO magnetic materials.

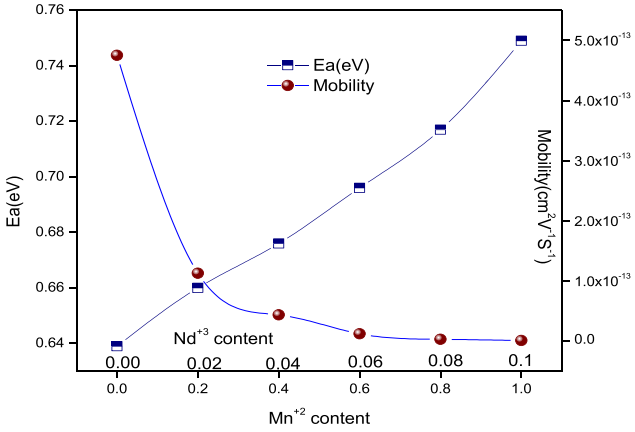

Fig. 5. A plot of activation energy against Mn-Nd content in comparison with drift mobility.

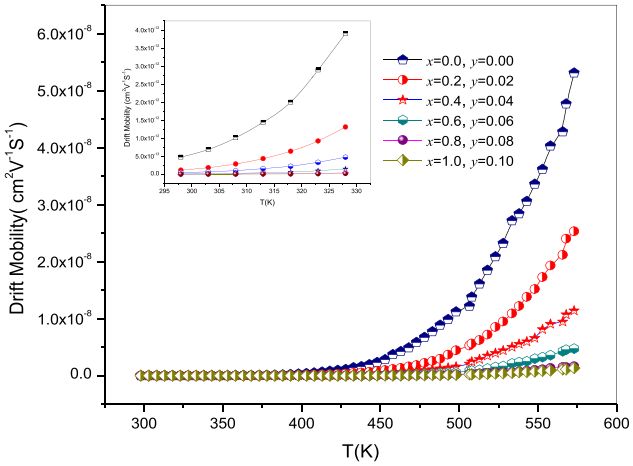

Fig. 6. Mobility as a function of temperature of Mn-Nd co-substituted CFO magnetic materials.

3.3.3. Drift mobility

The charge carrier's mobility was calculated by using the experimental data of electrical resistivity for all the samples. The drift mobility is related to the temperature by the following relation:

$$\mu_d = \mu_o \exp\left(-\frac{E_a}{k_B T}\right) \quad (13)$$

where μ_0 is pre-exponential constant, k_B is Boltzmann constant and E_a is the activation energy for mobility of ions. The charge carrier mobility values for different compositions are given in Table 2. The electrical conductivity data, activation energy and drift mobility are in good agreement with each other which can be seen from the Table 2. The mobility is maximum for un-doped material which decrease with the increase in substituent contents and is minimum for the x=1.0 and y=0.1. Such low values of mobility have already been reported by several researchers [33–36]. The variation of mobility with temperature is shown in Fig. 6. It can be seen from the figure that the charge carrier mobility values increase continuously with the increase of temperature. The increase in mobility with temperature suggests that the conduction in these materials is due to the hopping of electrons from Fe^{2+} to Fe^{3+} and holes transfer from Co^{3+} to Co^{2+} and Mn^{3+} to Mn^{2+}. Similar behavior has also been reported by other researchers [35,36].

3.4. Dielectric properties

3.4.1. High frequency dependent dielectric constant

Fig. 7 shows the effect of applied frequency on the dielectric constant (ε′) in the frequency range of 1 MHz–3 GHz. It can be seen that with the increase of frequency the value of dielectric constant decreases continuously. The decrease of dielectric constant with frequency is a normal behavior of the multiferroic materials and extensively examined by other researchers [37,38]. This trend of large values of dielectric constant (ε′) at lower frequency may be attributed to the following reasons: predominance of species like Fe^{2+} ions, oxygen vacancies, grain boundary defects, interfacial dislocation pile ups and voids [39,40]. The dielectric constant decrease sharply at low frequency as compared to that at high frequency and become almost constant on further increasing the frequency. The observed high dielectric constant at low frequencies might be attributed to the Maxwell–Wagner type of

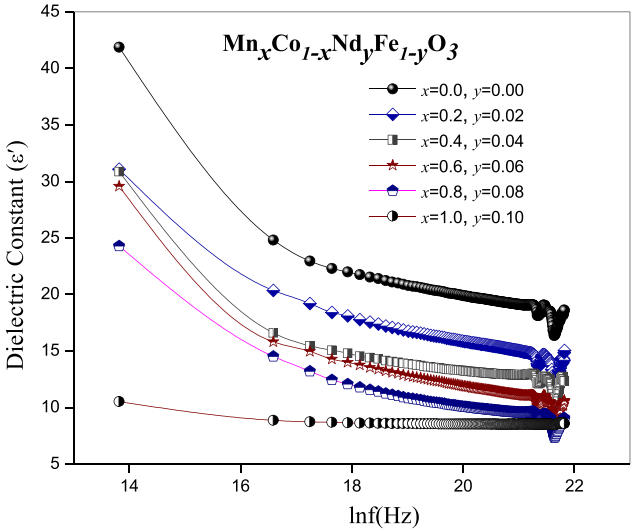

Fig. 7. Variation in dielectric constant with frequency of Mn-Nd co-substituted CFO magnetic materials.

interfacial polarization mechanism that plays very important role in these types of nano-crystallites. The interfaces between the ferroelectric and ferromagnetic phases which have significantly different conductivities cause an additional polarization that is termed as the interfacial polarization which boosts the dielectric constant [41]. Interfacial polarization responds very slowly to the external field hence it dominates in the low frequency region and has no significant contribution in the high frequency region (1 MHz–3 GHz). The lowering of the dielectric constant with increasing frequency is attributed to the fact that under the influence of external electric field the dielectric material exhibits induced electric moment. But as the frequency increases the polarization of induced moments or electronic exchange between Fe^{2+} and Fe^{3+} ions could not synchronize with the frequency of applied electric field [42]. The charge carriers in a dielectric took a finite time to line up parallel to an alternating applied electric field. When the frequency of the applied ac field increased and at certain point the space charge carriers could not follow the applied field and the charge carriers lagged behind the applied field. As a result the dielectric constant of a material is decreased. Resonance peaks are observed beyond the frequency of 2.4 GHz. Mainly there are two relaxation phenomenons in these materials. At low frequency the relaxation is due to interfacial polarization while at higher frequency is related to ionic relaxation. These peaks appeared when the jumping frequency of electron hopping between Fe^{2+} and Fe^{3+} become equal to the frequency of applied ac field. The other ions such as Mn also contribute to this resonance phenomenon as it also changes from Mn^{2+} to Mn^{3+}.

3.4.2. *High-frequency-dependent dielectric dissipation factor*

The variation of dielectric dissipation factor (ε″) versus frequency is shown in Fig. 8. The results show that the ε″ reduced with the increasing applied field frequency. It has been observed that grain boundaries are responsible for high value of dissipation factor at lower frequency. Similarly the energy loss has also been observed high in the lower frequency regime because additional energy was necessarily required for electron exchange between Fe^{3+} and Fe^{2+} ions. At higher frequency region the value of ε″ has been observed to be very small due to grains. This exhibit that small amount of energy is enough for electronic conversation between Fe^{3+} and Fe^{2+} in the grains. Hence the observed energy loss is relatively small. The temperature of the material is raised due to the internal resistance of the movement of each dipole which is responsible for the power loss in the dielectric material. Therefore, the materials with low resistivity (high conductivity) demonstrated high dielectric losses and vice versa [43]. The Maxwell-Wagner's model and Koops phenomenological theory are responsible for the phenomenon of dielectric dispersion in these materials. The appearance of resonance peaks in Fig. 8 can be explained that if an ion has two equilibrium states U and W having equal potential energies separated by a potential barrier, this situation corresponds to the same jumping probability of an ion i.e. from U to W and from W to U. The natural frequency of jump is the frequency at which an ion changed its position between the two equilibrium states U and W. When the frequency of external applied ac field becomes equal to the natural frequency of ions then transfer of maximum electrical energy to the oscillating ions and a sharp increase of power loss take place and as a result the phenomenon of resonance occurs [44].

3.4.3. *High-frequency-dependent dielectric tangent loss (tanδ)*

Fig. 9 shows the variation of dielectric tangent loss (tan δ) as a function of applied field in the range of 1 MHz–3 GHz. The behavior of dielectric tangent loss (tan δ) is same as that of ε′ and ε″.

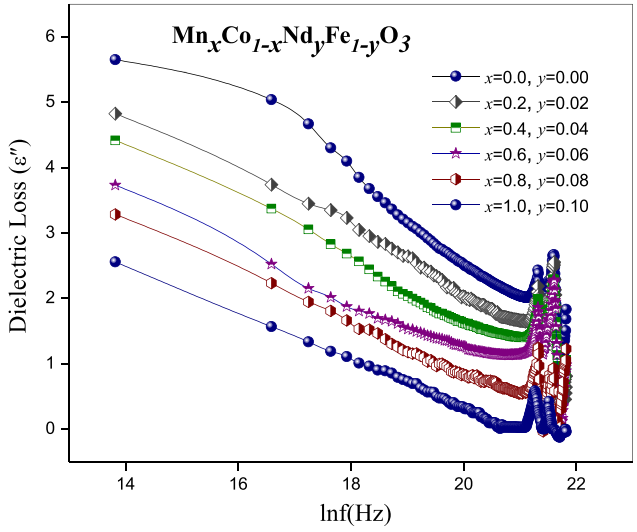

Fig. 8. Variation in dielectric loss with frequency of Mn-Nd co-substituted CFO magnetic materials.

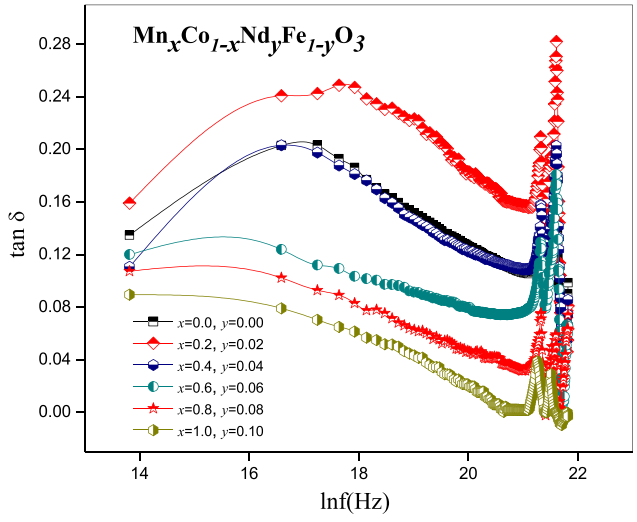

Fig. 9. Variation in dielectric loss tangent with frequency of Mn-Nd co-substituted CFO magnetic materials.

The decreased dielectric tangent loss (tan δ) became almost independent at higher frequencies. The phenomenon of dielectric dispersion in multiferroics is based on Maxwell-Wagner's model [41] and Koops phenomenological theory. The resonance peak is due to matching of frequency of applied frequency with that of transfer of electrons in iron ions. The condition for observing the maximum dielectric loss of a dielectric material is given by:

$$\omega_{\max}\tau = 1 \text{and} \tau = \frac{1}{\omega_{max}} \tag{14}$$

where $\omega = 2\pi f_{max}$. The relaxation time τ is related to the jumping probability per unit time p as

$$\tau = \frac{1}{2}p \tag{15}$$

According to the Eq. (14), the Debye relaxation process occurs when the jumping rate of electrons between Fe^{2+} and Fe^{3+} become nearly equal to the frequency of the applied ac field.

It has been observed that the value of dielectric constant decreases more quickly as the frequency increases as compared to dielectric loss. These variations in the values of dielectric parameters can be best justified by the following relation:

$$\varepsilon' = \varepsilon_\infty + \frac{\varepsilon_s - \varepsilon_\infty}{1 + \omega^2\tau^2} \tag{16}$$

$$\varepsilon'' = \frac{(\varepsilon_s - \varepsilon_\infty)\omega\tau}{1 + \omega^2\tau^2} \tag{17}$$

where τ, ε_s and ε_∞ are the relaxation time, dielectric constant at very low and very high frequency, respectively and "ω" is the angular frequency. Eq. (16) reveals that dielectric constant (ε′) decreases more rapidly with increasing frequency, as (ε′) is proportional to the $1/\omega^2$. Similarly, Eq. (17) suggests that decrease of (ε″) is comparatively low because (ε″) is proportional (1/ω). Therefore, the comparatively sharp decrease of the (ε′) than that of (ε″) in the given frequency range may favor the existence of peaks in the tan δ(*f*) plot as shown in Fig. 9. Moreover, a reasonable clarification for existence of the peaks in plot of tan δ against the frequency can be given on behalf of the previous hypothesis that in multiferroics a strong correspondence exists between the dielectric polarization and the conduction mechanism. In this case the peaks detection in tan δ(*f*) curves takes place only when the external electric field becomes equal to the hopping frequency of charge carriers.

Fig. 10 shows comparison between the variation of dielectric constant at 1 GHz and DC resistivity with Mn-Nd contents. The decrease in dielectric constant with increase in Mn-Nd contents is attributed to increase in resistivity of the samples. This increase in electrical resistivity and decrease in dielectric constant suggest that the synthesized materials can be used in microwave devices fabrications.

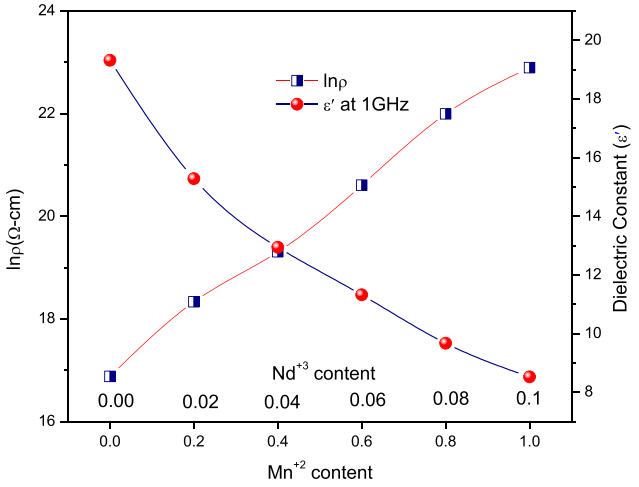

Fig. 10. Room temperature resistivity and dielectric constant versus dopant concentration.

3.4.4. *High-frequency dependent AC electrical conductivity (σ_{AC})*

Fig. 11 shows the variation of ac electrical conductivity (σ_{AC}) versus frequency (1 MHz–3 GHz). The ac conductivity (σ_{AC}) of the nano-crystallites materials depend on the hopping of electrons between Fe^{3+} and Fe^{2+} ions at the octahedral sites. As the frequency increases then the hopping of electrons between Fe^{3+} and Fe^{2+} at octahedral site also increases. As a result the ac conductivity increases. The plot of log(σ_{AC}) versus log(ω) is shown in Fig. 12. The exponent 'n' was calculated from the linear part of the plot between log(σ_{AC}) and log(ω) by using the equation:

$$\sigma_{AC} = B\omega^n \tag{18}$$

It has been reported that the value of 'n' lies between 0 and 1. When n = 0, the electrical conduction is frequency independent or dc conduction and for $n \leq 1$, the conduction is frequency dependent or ac conduction. In the present study, the value of exponent

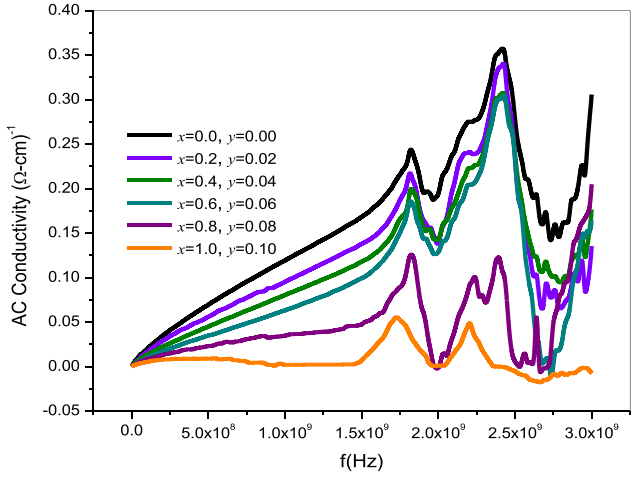

Fig. 11. AC electrical conductivity with frequency of Mn-Nd co-substituted CFO magnetic materials.

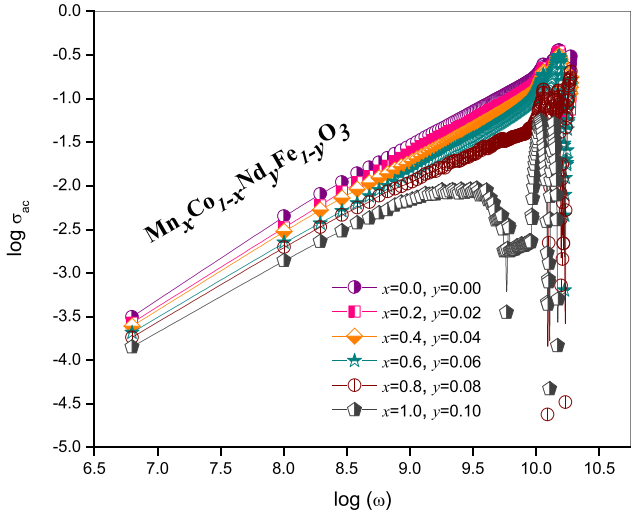

Fig. 12. Log of AC electrical conductivity as a function of log(ω) of Mn-Nd co-substituted CFO magnetic materials.

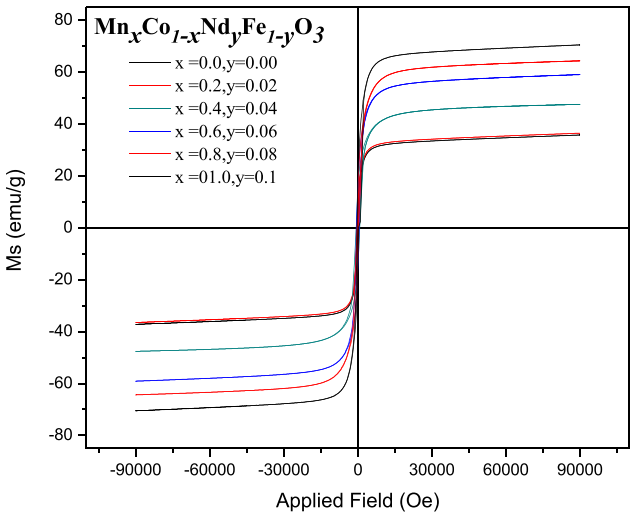

Fig. 13. Hysteresis loops for Mn-Nd co-substituted CFO magnetic materials at room temperature.

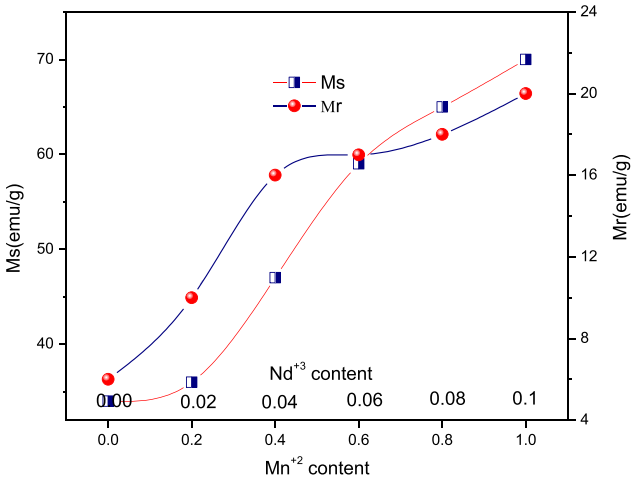

Fig. 14. variation of saturation magnetization and remanance as a function of Mn-Nd content.

'n' varies between 0.70 and 0.84 (Table 2) which suggests that the conduction phenomenon in the present samples follows hopping conduction mechanism.

3.5. Magnetic properties

The magnetic properties such as saturation magnetization (M_s), remanence (M_r) and coercivity (H_c) has been determined from the hysteresis loops and are shown in Fig. 13. The hysteresis loops are not wide which indicate that these are soft multiferroics. The variation of saturation magnetization and remanence with Nd-Mn contents are shown in Fig. 14. It is clear from the figure that saturation magnetization and remanence increase while coercivity decreases with the increase in substituent contents. The magnetization of the magnetic materials depends upon the number of unpaired electrons. According to the electronic configuration the Mn^{2+} and Nd^{3+} have 5 and 3 unpaired electrons, respectively and the Fe^{3+} and Co^{2+} also have magnetic moment of $5\mu_\beta$ and $3\mu_\beta$. So the net effect of unpaired electrons in substituted and un-substituted material is same. The increase in magnetization in the substituted materials can be explained on the basis of distortion in the structure. It has been reported that substitution of large ionic radii elements can cause distortion in the structure which may improve the saturation magnetization [45]. In the present investigation, the substituents i.e. Nd and Mn cause to increase the cell volume as evidenced by the XRD analysis which results in the increase in saturation magnetization as well as remanence. The substituted samples contain manganese which can be change from Mn^{2+} to Mn^{3+} and to maintain the overall electroneutrality the Fe^{3+} also convert to Fe^{2+} which also cause the distortion in the local structure. The increase in manganese content increases the distortion which causes to increase the saturation magnetization. The increase in saturation magnetization with substituents suggests that these materials can be used for the applications in high density recording media because such devices required the magnetization as high as possible. The value of coercivity decreases from 705 to 262 Oe with the increase in Nd–Mn contents as shown in Table 2. The decrease in coercivity is due to the increase in the average particle size of the materials by substitution of Nd-Mn concentration. The other reason for the decrease in coercivity may be due to decrease in anisotropy constant with the Nd–Mn contents. According to Li et al. [46] the longitudinal magnetic recording media used in industries requires high enough coercivity (600 Oe). If coercivity is too high (above 1200 Oe) the materials can be used for the perpendicular recording media which is developing new technology in the magnetic recording media applications. In the present work, the coercivity is in the range of 262–705 Oe, so the materials can be applicable in the longitudinal magnetic recording media applications.

4. Conclusion

The economical sol-gel auto-combustion method has been employed for the synthesis of Mn-Nd substituted perovskite structure materials. The XRD confirmed the formation of single phase while SEM images revealed spherical particles which turned to rod shaped with the increase in Mn-Nd contents. The DC electrical resistivity and activation energy increase while drift mobility, dielectric constant, dielectric loss and dielectric loss factor decrease with the increase in substituent cations. The increase in DC electrical resistivity has been explained on the basis of site occupancy of the substituents. All the dielectric parameters decrease with the increase in frequency which was explained on the basis of Wagner theory. The saturation magnetization and remanence increase with the increase in Nd-Mn contents while the coercivity decreased. The increase in DC resistivity while decrease in dielectric constant make the synthesize materials suitable for microwave devices applications. The values of coercivity and saturation magnetization suggest that these materials are also suitable for the longitudinal magnetic recording media devices fabrications.

References

[1] A. Ali, M.U. Islam, M.N. Ashiq, H.M. Khan, M.A. Iqbal, M.N. Haq, Mater. Res. Bull. 49 (2014) 338–344.
[2] X. Mao, W. Wang, X. Chen, Y. Lu, Appl. Phys. Lett. 95 (2009) 082901.
[3] M. Fiebig, J. Phys. D: Appl. Phys. 38 (2005), R123.
[4] T. Ju, Y. Cai, G.Y. Guo, Z.Y. Li, Phys. Rev. B 75 (2007) 064419.
[5] M. Kumar, K.L. Yadav, Appl. Phys. Lett. 91 (2007) 242901.
[6] Y. Bai, F. Xu, L. Qiao, J. Zhou, J. Alloy. Compd. 473 (2009) 505–508.
[7] S.Y. Tong, J.M. Wu, M.J. Tung, W.S. Ko, Y.T. Huang, Y.P. Wang, J. Alloy. Compd. 525 (2012) 143–148.
[8] J. Chand, S. Verma, M. Singh, J. Alloy. Compd. 552 (2013) 264–268.
[9] N.Y. Mostafa, M.M. Hessien, A.A. Shaltout, J. Alloy. Compd. 529 (2012) 29–33.
[10] M. Ahmad, I. Ali, R. Grössinger, M. Kriegisch, F. Kubel, M.U. Rana, J. Alloy. Compd. 579 (2013) 57–64.
[11] A. Pradeep, P. Priyadharsini, G. Chandrasekaran, J. Mater. Chem. Phys. 112 (2008) 572–576.
[12] T.J. Shinde, A.B. Gadkari, P.N. Vasambekar, J. Alloy. Compd. 513 (2012) 80–85.
[13] A. Verma, O. Thakur, C. Prakash, T. Goel, R. Mendiratta, Mater. Sci. Eng. B 116 (2005) 1–6.

[14] A.B. Nawale, N.S. Kanhe, K.R. Patil, S.V. Bhoraskar, V.L. Mathe, A.K. Das, J. Alloy. Compd. 509 (2011) 4404–4413.
[15] Y. Kinemuchi, K. Ishizaka, H. Suematsu, W. Jiang, K. Yatsui, Thin Solid Films 407 (2002) 109–113.
[16] N. Rezlescu, E. Rezlescu, P.D. Popa, C. Doroftei, M. Ignat, Compos.: Part B 60 (2014) 515–522.
[17] N.A. Merino, B.P. Barbero, P. Grange, L.E. Cadus, J. Catal. 231 (2005) 232–244.
[18] S. Rayaprol, S.D. Kaushik, P.D. Babu, V. Siruguri, Proceedings of the 57th DAE Solid State Physics Symposium, in: AIP Conference Proceedings, vol. 1512, 2013, pp. 1132 – 1133.
[19] T.I. Hua, R. Sundari, J. Fund. Appl. Sci. 8 (2012) 149–154.
[20] B. Kucharczyk, W. Tylus, Appl. Catal. A 335 (2008) 28–36.
[21] N. Lampis, C. Franchini, G. Satta, A.G. Lehmann, S. Massidad, Phys. Rev. B 69 (2004) 064412.
[22] J. Xu, H. Ke, D. Jia, W. Wang, Y. Zhou, J. Alloy. Compd. 472 (2009) 473–477.
[23] B. Ahmad, A. Mahmood, M.N. Ashiq, M.A. Malana, M.N. Haq, M.F. Ehsan, M. F. Warsi, I. Shakir, J. Alloy. Compd. 590 (2014) 193–198.
[24] M.A. Ahmed, N. Okasha, M. Oaf, R.M. Kershi, J. Magn. Magn. Mater. 314 (2007) 128–134.
[25] W.E. Lee, W.M. Rainforth, Ceramic Microstructures: Property Control 335 by Processing, Kluwer Academic Publishers, 1994.
[26] N. Rezlescu, E. Rezlescu, J. Solid State Commun. 88 (1993) 139–141.
[27] N. Rezlescu, E. Rezlescu, P.D. Popa, L. Rezlescu, J. Alloy. Compd. 275–277 (1998) 657–659.
[28] N. Rezlescu, E. Rezlescu, C. Pasnicu, M.L. Craus, J. Phys. Condens. Matter 6 (1994) 5707–5716.
[29] G.L. Sun, J.B. Li, J.J. Sun, X.Z. Yang, J. Magn. Magn. Mater. 281 (2004) 173–177.
[30] D. Ravinder, P.V.B. Reddy, Mater. Lett. 57 (2003) 4344–4350.
[31] M.J. Iqbal, M.N. Ashiq, Scr. Mater. 56 (2007) 145–148.
[32] A.M.M. Farea, S. Kumar, K.M. Batoo, A. Yousef, C.G. Lee, J. Alloy. Compd. 469 (2009) 451–457.
[33] T.M. Meaz, S.M. Attia, A.E. Ata, J. Magn. Magn. Mater. 257 (2003) 296–305.
[34] A.V.R. Reddy, G.R. Mohan, B.S. Boyanov, D. Ravinder, Mater. Lett. 39 (1999) 153–165.
[35] K.V. Kumar, D. Ravinder, Int. J. Inorg. Mater. 3 (2001) 661–666.
[36] D. Ravinder, A.V.R. Reddy, Mater. Lett. 38 (1999) 265–269.
[37] D. Ravinder, Mater. Lett. 43 (2000) 129–138.
[38] M.J. Iqbal, M.N. Ashiq, P.H. Gomez, J.M. Munoz, J. Magn. Magn. Mater. 320 (2008) 881–886.
[39] Z. Hu, M. Li, Y. Yu, J. Liu, L. Pei, J. Wang, X. Liu, B. Yu, X. Zhao, Solid State Commun. 150 (2010) 1088–1091.
[40] M.G.F. Silva, M.A. Valente, Mater. Chem. Phys. 132 (2012) 264–272.
[41] K.W. Wagner, Ann. Phys. (Liepzig) 345 (1913) 817.
[42] J.C. Maxwell, Electricity and Magnetism, Oxford University Press, New York 1973, p. 828.
[43] S.C. Watawe, B.D. Sarwede, S.S. Bellad, B.D. Sutar, B.K. Chougule, J. Magn. Magn. Mater. 214 (2000) 55–60.
[44] M. Chanda, Science of Engineering Materials, 3, The Macmillan Company of India Ltd., New Delhi 1980, p. 103.
[45] V.A. Khomchenko, D.A. Kiselev, M. Kopcewicz, M. Maglione, V.V. Shvartsman, P. Borisov, W. Kleemann, A.M.L. Lopes, Y.G. Pogorelov, J.P. Araujo, R. M. Rubinger, N.A. Sobolev, J.M. Vieira, A.L. Kholkin, J. Magn. Magn. Mater. 321 (2009) 1692–1698.
[46] Y. Li, R. Liu, Z. Zhang, C. Xiong, Mater. Chem. Phys. 64 (2000) 256–259.